Photoinduced Surface Electric Fields and Surface Population Dynamics of GaP(100) Photoelectrodes

Tong Zhang[1,2,3#], Zhi-Chao Huang-Fu[3#], Yuqin Qian[3], Hong Gao[1,2]*, Jesse B. Brown[3], and Yi Rao[3]*

[1]Beijing National Laboratory for Molecular Sciences and State Key Laboratory of Molecular Reaction Dynamics, Institute of Chemistry, Chinese Academy of Sciences, Beijing 100190, China
[2]University of Chinese Academy of Sciences, Beijing 100049, China
[3]Department of Chemistry and Biochemistry, Utah State University, Logan, UT, 84322
[#]These authors contributed equally to this work

Abstract

Gallium phosphide (GaP) photoelectrodes have received remarkable focus due to their applications in photocatalysis and photoelectrocatalysis of CO_2 reduction reactions. Understanding the dynamical mechanisms of surfaces of photoelectrodes is essential in improving their working efficiencies in any application. However, knowledge of photoinduced surface dynamics of these materials is lacking. Here we investigate surface dynamics of *n*-type and *p*-type GaP(100) semiconductors by utilizing time-resolved electronic sum frequency generation (TR-ESFG). Transient ESFG spectra showed that four surface states in both *n*- and *p*-type GaP(100) were involved in subsequent kinetics. Transient spectral signatures of the surface states showed that photoexcited electrons move towards the surface regions for the p-type GaP, while photoexcited holes move to the surface regions for *n*-type GaP. These carriers first build up surface electric fields, resulting fluence-dependent band flattening. The buildup rates of the surface electric fields were found to be on the order of 2.86 ± 0.30 ps^{-1} for *n*-type and 2.50 ± 0.25 ps^{-1} for *p*-type. Subsequently, a relatively slow process occurs, being attributed to population dynamics of surface states dependent upon applied fluences. We found that surface population behaves as a bimolecular process with rates of 0.020 ± 0.002 cm^{2}s^{-1} for *n*-type, and 0.035 ± 0.002 cm^{2}s^{-1} for *p*-type GaP. The four surface states, shallow and deep for both *n*- and *p*-type GaP(100), were found to be involved in both surface electric fields and surface carrier populations, contrary to previous hypotheses. Our time-resolved surface-specific approach provides unique information on surface dynamical behaviors of photoelectrodes under ambient conditions.

*Corresponding authors: Y.R. (yi.rao@usu.edu) and H.G. (honggao2017@iccas.ac.cn)

Introduction

The reductions of CO_2 through photocatalysis and photoelectrocatalysis can capture and convert it into useful organic products.[1-3] These photoinduced reactions are one of the strategies to mitigate the greenhouse effect and satisfy the growing global energy demand. Thus, these advantages have attracted concentrated attentions from both fundamental and applied sciences. Photoelectrode surfaces play a vital role in the photocatalytic reduction of CO_2.[1] Critical to the fundamental insights into the reaction, and thereby improving its conversion efficiency, is the understanding of ultrafast charge transfer processes and chemical reactivity at photoelectrode surfaces. For example, it has been hypothesized that surface properties of photoelectrodes and chemical intermediates during a reaction affect its pathways and yields of the photoinduced reaction of CO_2.[1-3] Despite the importance, understanding of photoelectrode surfaces is deficient. This is largely due to experimental difficulties in selectively probing such ultrafast processes in the semiconductor surface region under ambient conditions.

In photocatalytic and photoelectrocatalytic process, a semiconductor acts as a photoelectrode. For a semiconductor photoelectrode, free carrier densities create a space charge layer due to surface band bending, either a depletion or accumulation layer.[4-5] For example, a *p*-type photoelectrode with a depletion layer shows downward band bending. Surface states are formed due to intentional or unintentional doping or terminated bonds on semiconductor photoelectrodes. Different doping levels are related to the thickness of the depletion layer which decreases with increased doping, thus affecting the energy levels for surface states. Under illumination, a photoelectrode absorbs the incident photons equal to or higher than its bandgap energy (E_g) from the valence band (VB) to the conduction band (CB). The absorption of light generates electrons and holes in the photoelectrode. For *p*-type photoelectrodes, the photogenerated electrons act as minority carriers and migrate to the photoelectrode-electrolyte interface.[6-7] When the photoelectrode is immersed in an electrolyte, the surface is enriched by foreign chemical species which can introduce additional surface band bending and modulate surface states. From the fundamental point of view, a photon will be absorbed if its energy is at least that of the band gap of the excited semiconductor. This causes electrons to be excited to the CB, leading to holes in the VB. The carriers will then transfer to the surface of the photoelectrode, and transfer to the acceptor molecules. Subsequently, an oxidation or reduction process will begin.[8] The surface band-bending separates electron-hole pairs, allowing the liberated electrons to populate the surface states of the photoelectrode.[4, 9-12] Furthermore, not all separated electrons partition to the surface states successfully, and consuming portions of electrons reduces photocatalytic efficiency. In other words, ensuring that all separated electrons move to the surface and participate in a particular reaction is a critical factor for improving photocatalytic efficiency.

Surface states and other defects in photoelectrodes play an important role in photocatalytic and photoelectrocatalytic reaction processes.[13-16] Surface states are either localized or delocalized. Localized surface states can act as a trap for photogenerated electrons, which can inhibit the recombination of electrons and holes; thereby facilitating the separation and transport of carriers. On the other hand, delocalized surface states are still suitable for charge transport. According to energy levels in the band gap, surface states are categorized as either shallow or deep states. Shallow surface states are close to the band edges of the CB for n-type or the VB for p-type.[17] Deep surface states are located deeper within the band gap.[18-19] Shallow surface states can provide free carriers, while deep surface states are generally localized. Deep surface states can act as traps to facilitate recombination and reducing catalytic efficiency. Surface states can cumulatively enhance or weaken surface electric fields, further influencing carrier transfer at surfaces.[20-23] Surface electric fields can separate electron−hole pairs, which reduces the rate of recombination.[4] Dynamics of surface states are intimately related to charge recombination and charge separation at photoelectrode surfaces. Therefore, understanding the structure and dynamics of surface states is essential in the rational design of surface structures of photoelectrodes for the photocatalytic and photoelectrocatalytic reduction of CO_2 .

GaP semiconductors were demonstrated as a photoelectrode for the reduction of CO_2 into formic acid by Halmann and co-workers in 1978.[24] Since then, many groups applied GaP or modified GaP into photocatalysts and photoelectrocatalysts used for CO_2 reduction, providing better performance in catalytic reactions.[25-27] For example, Yoneyama and co-workers used *p*-type GaP as a photoelectrode in a lithium carbonate electrolytes to study CO_2 reduction.[28] They converted CO_2 to HCOOH, HCHO, and CH_3OH, and enhanced the current efficiency by adding 15-crown-5 into the electrolytes. Another example comes from Bocarsly and co-workers, who used *p*-type GaP and homogeneous pyridinium ions to achieve near 100% faradaic efficiencies for the reduction of CO_2 at potentials well below the standard potential.[27] Recently, Cronin and co-workers used atomic layer deposition to deposit a thin film of TiO_2 on *p*-type GaP(100) photoelectrodes to stabilize the GaP surface.[25] In their work, the formation of *p*-*n* junctions with the deposited *n*-type TiO_2 reduced the recombination of electron−hole pairs and improved the conversion efficiency of CO_2 into CH_3OH.

Different methods such as minority-carrier capture,[29] time resolved microwave conductivity,[30] photoemission spectroscopy[31] and pump/probe spectroscopy[32] have been used to study carrier dynamics of GaP. For example, Ujihara and co-workers[31] used photoemission spectroscopy to measure carrier relaxation times in GaP. They observed two peaks in the spectra of energy distribution curves, which are due to the accumulation of photoexcited electrons in the X valley and Γ valley. According to the ratio of the concentration of the electrons in X valley and Γ valley, they calculated carrier relaxation times. Faassen and co-workers[30] used time resolved microwave conductivity methods to study the charge carrier recombination dynamics of nano porous GaP and formulated a model to explain the observed transients. The charge carrier recombination was assumed to occur at the surface of GaP and the rates of which were determined by the band bending associated with the depletion layer. However, these non-surface specific methods cannot provide dynamics of surface states directly.

Second harmonic generation (SHG) and sum frequency generation (SFG), as second-order nonlinear optical spectroscopic techniques, are proven tools for surface and interface analysis due to their intrinsic surface selectivity.[33-69] Time-resolved second harmonic generation (TR-SHG)[70-87] and time-resolved electronic sum frequency generation (TR-ESFG)[88-93] have been used to study rotation dynamics, solvation dynamics, electron transfer, molecular relaxation, and so on. Zhu and co-workers used TR-SHG to study the mechanism of photoinduced charge separation at the interface of hybrid CuPc/GaAs[70], and semiconductor surfaces.[71] They found that competing charge separation processes existed in the GaAs/CuPc interface and that the space charge field of GaAs slows down hole injection to CuPc. Our early work demonstrated surface dynamics for *p*-type GaAs (100) with the development of time-resolved broadband ESFG.[92, 94-95] TR-ESFG could provide time-resolved spectral information about surface structures as well as charge transfer occurring at semiconductor surfaces.

In this work, we employed TR-ESFG to investigate the dynamics of transient surface electric fields and surface states for *n*-type and *p*-type GaP(100). Our purpose is to compare buildup dynamics of surface electric fields and population dynamics of surface states for the two different doped GaP(100).

Methods

A fundamental light centered at 800 nm with an output of 4.0 mJ output and a pulse duration of 100 fs was generated by a 1 kHz Ti-sapphire amplified laser system (Uptek solutions). A portion of 2.0 mJ of the fundamental light was used to generate a picosecond pulse from an etalon (SLS Optics). A smaller portion of 1.5 mJ was used to pump a broadband optical parametric amplifier (BOPA) to generate a shortwave IR pulse (SWIR). The spectra of the ps 800 nm and the SWIR are shown in Figure S1. A detailed description of design and implementation of the BOPA were reported in our previous work.[92, 94-95] The remaining portion of 0.5 mJ was used to generate a pump pulse of 400 nm by a Beta Barium Borate (BBO) crystal.

Figure 1(A) shows a schematic setup for time-resolved ESFG experiments. The picosecond 800 nm pulse of 40 μJ and the SWIR of 10 μJ were focused on a sample surface with spot sizes of 510 μm in diameter by a lens with 20 cm focal length at an incident angle of 60°, and 305 μm by a 15 cm focal length lens at an incident angle of 45°. The pump pulse of 400 nm was focused by a 40 cm focal length lens to a spot size of 490 μm at an incident angle of 37°. All three pulses were aligned into a single incident plane. A 1000 nm long-pass filter (Thorlabs) was used to remove the fundamental light and other light generated from the optics in the light path. The polarization combinations of ESFG signals, the picosecond, and the SWIR pulse were controlled by polarizers (Thorlabs) and half-wave plates (Thorlabs). The polarization of the pump pulse was set as P-polarized in the incident plane. A motorized translation stage (Klinger, UT100-100) was placed in the picosecond 800 nm path to change a time delay between the SWIR and picosecond pulses. The time delay between the pump and the SWIR was controlled by another motorized translation stage (Klinger, UT100-100). Azimuthal angles of samples were controlled by a motorized rotation stage (Newport, PR50CC). A 780 nm short-pass filter (Thorlabs) and a 445 nm long-pass filter (Thorlabs) were used to remove the fundamental light and other light from surroundings after samples.

An optical chopper of 500 Hz was placed in the light path of the 400 nm pump pulse to select pump-on, $I_{pump\text{-}on}(\omega, t)$, and pump-off, $I_{pump\text{-}off}(\omega)$, ESFG signals, which was synchronized with the 1 kHz laser system. The ESFG spectra for the pump-off are found in Figure S1. A single-axis Galvo mirror (Thorlabs) rotated up and down at an angle of 1.5°, followed by a vertically cylindrical lens (f=250 mm) and a horizontally cylindrical lens (f=100 mm). The former was used to image the pump-on and pump-off separately, and the latter to make sure that ESFG signals were spectrally resolved. ESFG signals were dispersed by a spectrometer (Kymera 328i-C, Andor Technology) and detected by a thermally cooled charge-coupled device (IDus DU420A-BVF, 1024×255, Andor Technology). Time-resolved ESFG spectra, $(I_{pump\text{-}on}(\omega, t)\text{-}I_{pump\text{-}off}(\omega))/I_{pump\text{-}off}(\omega)$, were sampled by a custom LabVIEW program. The instrumental response function of 200 fs was determined by mixing the 400 nm with the SWIR for SFG.

Both n-type GaP(100) S-doped 2-12 $\times 10^{17}$ cm^{-3} and p-type GaP(100) Zn-doped 4.0-5.2$\times 10^{17}$ cm^{-3} were purchased from MTI. Prior to experiments, the samples were cleaned in acetone.

Results & Discussion

Azimuth-dependent TR-ESFG. Experimentally, we found that transient ESFG signals depended upon azimuthal angles of the GaP crystals. Here, ϕ is defined to be an azimuthal angle, which is 0° when the [011] direction is along the X axis in the laboratory coordinates and the azimuthal rotation is counterclockwise, as shown in Figure 1(B). We have then excluded the possibility of preferential excitations by checking with depolarized and different polarized pumps, as shown in Figure S2. It is seen that the azimuth-dependent photoinduced ESFG signals are independent of pump polarization. The polarization of the pump was set to be P-polarized unless otherwise stated. Figure 1(C) shows azimuth-dependent transient PSS-polarized ESFG signals at 500 nm for n-type GaP(100) at a time delay of 90 ps under a 400 nm photoexcitation of 20 μJ/cm^2. The transient ESFG signals are shown to be positive below ca. 40°, a sharp change occurs near 45°, followed by negative signals, and a mirror symmetry exists from 90° to 180°. The entire pattern appears to have a 2-fold symmetry, with slight deviations near the local maxima. These azimuth-dependent patterns are independent of the probed wavelength.

To reveal azimuth-dependent transient ESFG signals, we shall deal with the origin of photoinduced responses from GaP surfaces. GaP(100) crystals possess a zinc blende structure $\bar{4}3m$ (T_d). Effective

second-order susceptibilities of the GaP(100) originate from bulk dipoles (anisotropic $\chi^{(*)}_{"\#,\%\&'(}$), surface dipoles (isotropic $\chi^{(*)}_{,\#,'(-}$ and anisotropic $\chi^{(*)}_{,\#,\%\&'(}$), and surface charges (isotropic $\chi^{(*)}_{,.,'(-}$ and anisotropic $\chi^{(*)}_{,.,\%\&'(}$). All the anisotropic parts follow a 2-fold symmetry in the surface plane. $\chi^{(*)}_{"\#,\%\&'(}$ were found to contribute to non-resonant responses, independent of frequency or wavelength, as shown in Supporting Information. Thus, azimuth-dependent steady-state ESFG intensities take the form of

$$I_{!"\#\$}(\omega,\phi) \propto \left(\frac{\chi^{()}_{!",\$\%\&'\&'()^*}}{+,\Delta.+} + \chi^{()}_{"0,23,(}(\omega)cos2\phi + \chi^{()}_{"6,23,(}(\omega)cos2\phi + \chi^{()}_{"0,,('}(\omega) + \chi^{()}_{"6,,('}(\omega)\right)^{)}. \quad (1)$$

Experimentally, it is hard to differentiate $\chi^{(*)}$ from surface dipoles and surface charges. We further simplify Equation (1) into

$$I_{!"\#\$}(\omega,\phi) \propto \left(\frac{\chi^{()}_{!",\$\%\&'\&'()^*}}{+,\Delta.+} + \chi^{()}_{"06,23,(}(\omega)cos2\phi + \chi^{()}_{"06,,('}(\omega)\right)^{)}. \quad (2)$$

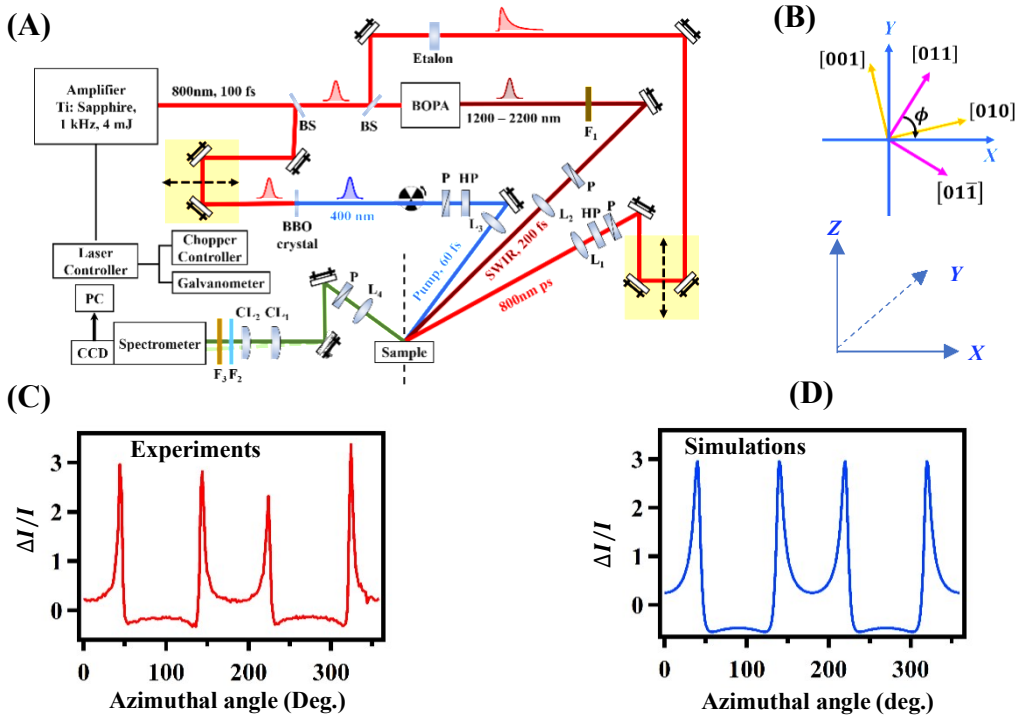

Figure 1. (A) A schematic setup for time-resolved ESFG spectroscopy. L_1: 20 cm lens; L_2: 15 cm lens; L_3: 40 cm lens; L_4: 10 cm lens CL_1: vertically cylindrical lens; CL_2: horizontally cylindrical lens; F_1: 1000 nm long-pass filter; F_2: 445 nm long-pass filter; F_3: 780 nm short-pass filter; BS: beam splitter; P: polarizer; HP: half-wave plate; (B) ϕ is 0° when the [011] direction is along the *X* axis in the laboratory coordinates and the azimuthal rotation is counterclockwise; (C) Experiential results of azimuth-dependent transient ESFG for *n*-type GaP(100). (D) Numerical simulations of azimuth-dependent transient ESFG for *n*-type GaP(100), based on Eq. S(1).

We first hypothesize that bulk susceptibility, $\chi^{(*)}_{ijk,\%\&'(}$, remains unchanged while surface responses change significantly under photo-illumination. Transient ESFG change, $\Delta\chi^{(*)}_{ijk}(\omega,t)$, is hypothesized to come mainly from those of surface electric fields or surface voltages, instead of surface dipoles. The changes in surface dipoles are assumed to be negligible since the values of changes are greater than or comparable to $\chi^{(*)}_{ijk}$. We further consider that $\Delta\chi^{(*)}_{ijk}(\omega,t)$ is linearly proportional to the changes in surface electric fields, $\Delta E_{ijk}(\omega,t)$, or surface voltages, $\Delta V_{ijk}(\omega,t)$. Time-dependent change ratios in ESFG, $\frac{I_{SF}(t)-I_{SF}}{I_{SF}}(\omega,\phi,t)=\frac{\Delta I}{I}(\omega,\phi,t)$, deal with time evolution of electric fields, carrier dynamics, recombination, and other intermolecular interactions occurring at surfaces and interfaces. A detailed derivation of $\frac{\Delta I}{I}(\omega,\phi,t)$ can be found in the Supporting Information. Briefly, azimuth-dependent time-resolved ESFG takes the form of

$$\frac{\Delta I}{I}(\omega,\phi,t)\approx\frac{\left(\chi^{(2)}_{eff,\$\%\&'}(=)\&'()*+\chi^{(2)}_{eff,-",\&'.}(=)?:\chi^{(2)}_{eff,-}(=,@)\right)^{2}}{\left(\chi^{(2)}_{eff}\&'()*B\right)^{2}+\left(\chi^{(2)}_{eff,\$\%\&'}(=)\&'()*+\chi^{(2)}_{eff,-",\&'.}(=)B\right)^{2}}\propto R(\omega,\phi)\Delta E_{ijk}(\omega,t)\propto R(\omega,\phi)\Delta V_{ijk}(\omega,t) \quad (3)$$

where $R(\omega,\phi)$ denotes the time-independent pre-factor. Figure S3 shows numerical simulations of $R(\omega,\phi)$ as a function of azimuthal angles for both *n*-type and *p*-type GaP(100), by setting $\chi^{(*)}_{ijk}$, $\chi^{(*)}_{ijk,\%\&'(}(\omega)$, and $\chi^{(*)}_{ijk,'(-}(\omega)$ with the values from steady-state ESFG measurements, as shown therein. It is seen that the azimuth-dependent pre-factor, $R(\omega,\phi)$, varies dramatically with azimuthal angle in both magnitude and sign. Thus, one should take the pre-factor into account in the interpretation of time-resolved ESFG spectra and time traces.

To validate our theoretical analysis, we conducted numerical simulations of azimuth-dependent transient ESFG signals for GaP(100). A detailed description of the numerical simulations can be found in the Supporting Information. The values for $\chi^{(*)}_{ijk}$, $\chi^{(*)}_{ijk,\%\&'(}$, and $\chi^{(*)}_{ijk,'(-}$ were adopted from our steady-state ESFG experimental results, as shown in Supporting Information. Figure 1(D) presents simulation results of azimuth-dependent transient PSS-polarized ESFG signals for *n*-type GaP(100), based on Eq. S(1). These numerical calculations are qualitatively consistent with those in Figure 1(C).

These results supported our hypothesis and have several implications: a) Bulk contributions, $\chi^{(*)}_{ijk}$, in the photoinduced ESFG are negligible; b) Transient spectra at any azimuthal angles reflect surface responses; c) $R(\omega,\phi)$ affects patterns of azimuth angle-dependent ESFG via variations of spectral signature and magnitude; d) Transient spectral signatures and magnitudes are not directly related to ground state bleaching or excited state absorption, unlike in transient ESFG experiments of molecular systems;[96-97]; e) For surface-dominant directions in static ESFG, higher-order effects occur near ϕ = (2n-1)×$\frac{2}{3}$ (n: integers) in transient ESFG. Thus, kinetic behaviors along these directions are not representative of time evolution of surface responses. We further analyzed how $\Delta\chi^{(*)}_{ijk}(t)$ introduces a non-negligible nonlinear term in Eq. S(1). Considering that the detection sensitivity of the transient ESFG varies with azimuthal angles, we chose to carry out our TR-ESFG experiments at ϕ=20° for *n*- and *p*-type GaP(100).

TR-ESFG spectra and kinetics for *n*- and *p*-type GaP(100). To compare transient surface behaviors for different doped GaP(100), we implemented TR-ESFG experiments under photoexcitation of 10 μJ/cm^2. Figure 2 shows time-resolved ESFG spectra and kinetic traces at ϕ = 20° for *n*- (left) and *p*-type (right) GaP(100) under the PSS polarization combination. Both the PSS and SPS provided similar results. Only

the transient spectra and kinetics for PSS are discussed in the rest of this work, unless otherwise stated. It is seen that transient ESFG signals exhibit positive and negative signs for *n*-type and *p*-type GaP(100), respectively. To further understand transient spectral signatures, we compared time-resolved ESFG spectra at different azimuthal angles for *n*- and *p*-type GaP(100), as displayed in Figure S4. These results show initial upward rise patterns, so-called "**M**"-shape, for *n*-type, while those downward fall pattern, so-called "**W**"-shape for *p*-type. Based on Eq. (3), the sign of $\Delta\chi^{(*)}_{,,}(\omega,t)$ was found to be positive for *n*-type and negative for *p*-type GaP(100). In other words, photoinduced ESFG signals increase for *n*-type and decrease for *p*-type GaP(100) upon photoexcitation, suggesting that surface electric fields or surface voltages get bigger for *n*-type and smaller for *p*-type crystals. Thus, transient ESFG spectral signatures are good indicators for the identification of changes in surface electric fields or surface voltages of semiconductors under non-equilibrium conditions.

All collected transient ESFG spectra cover from 470 nm to 540 nm. The transient ESFG spectra are generally broad. In an effort to obtain physically meaningful peaks, we used constraints while fitting ESFG spectra. The constraints were obtained from our static-state ESFG experiments, as shown in Figure S1, since they are from the same surface states in the two cases. Stead-state ESFG spectra show three peaks for both *n*-type and *p*-type GaP(100) due to the narrower spectral region. The positions of the three peaks from static-state ESFG spectra gave the constraints for fittings of the transient spectra. For *n*-type GaP(100), four positive peaks are located at around 478 nm, 494 nm, 514 nm, and 524 nm. These four ESFG peaks were assigned to the transitions from the VB to surface states. The peak at 478 nm is closer to the CB, while the other three peaks lie deeper within the bandgap. Transient spectra at 1 ps, 5 ps, 20 ps, and 81 ps show no difference. For *p*-type GaP(100), there are also four negative peaks located at around 477 nm, 489 nm, 507 nm, and 521 nm. These four peaks were attributed to the transitions from surface states to the CB. The peak at 477 nm is closer to the VB, while the other three peaks are farther away and deeper. The transient ESFG spectra for *p*-type GaP(100) show no difference at the four time delays. We also noticed that the peaks at 494 nm (*n*-type) and at 489 nm (*p*-type) are much broader than others. These differences likely originate from the distinct diffusive nature of the four surface states. It is noted that the change ratios, $\Delta I/I$, for the four peaks of *n*-type are more than twice those of the corresponding peaks for *p*-type. This is due to the fact that the pre-factor, $R(\omega,\phi)$ for the latter is almost twice that of the former. As a result, the values of $\Delta\chi_{,,}^{)}$ (t=50 ps) are comparable in both of the cases.

ESFG signals probe electronic transitions, instead of vibrational transitions. The ESFG signals of GaP come from bulk dipoles, bulk quadrupoles, surface dipoles, surface quadrupoles, and surface charges. However, the quadrupole contributions to SFG signals is much smaller than the dipole contributions. Therefore, the bulk quadrupoles and surface quadrupoles were assumed to be negligible. In terms of ESFG spectra, electronic transitions are dominated by surfaces. Bulk dipoles contribute to non-resonant signals. All these peaks were suggested to originate primarily from transitions of surface states for the GaP(100) crystals.

All the kinetic traces for the four peaks of both shallower and deeper surface states exhibit two components: one fast and one slow for both dopings. The time constants of the fast component for the four transitions are slightly different, on the orders of 0.30 - 0.40 ps for *n*-type and 0.34 - 0.45 ps for *p*-type. On the other hand, the time constants of the slow component for the four transitions are 5.00-7.88 ps for *n*-type at 514 nm and 3.00-4.00 ps for *p*-type at 507 nm. It is noted that a very slow relaxation process occurs

after the surface polpuations. Such a slow process is due to surface recombination of carriers. The time scale of such a recombination is as long as nanoseconds or above, which is beyond our scope here. The question arises of how we assign the two dynamical processes for *n*- and *p*-type GaP.

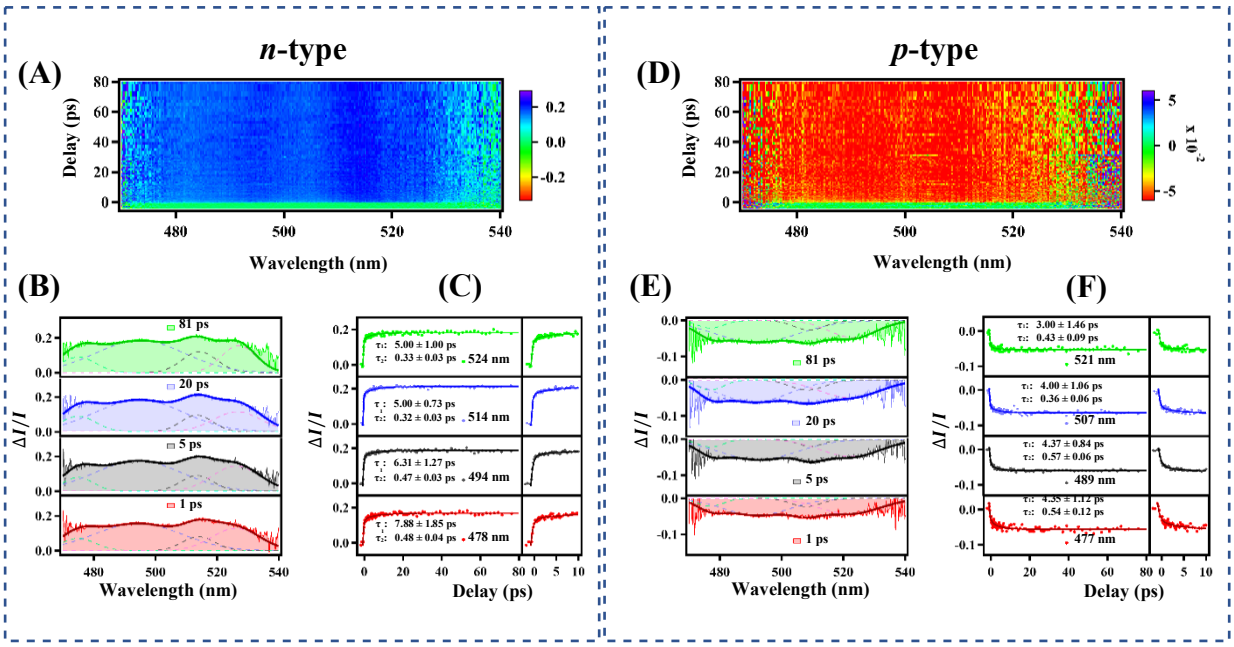

Figure 2. Pseudo-color 2D plot of transient ESFG spectra under PSS for *n*-type (A) and *p*-type (D) GaP(100) at ϕ = 20°. The transient spectra for 1 ps, 5 ps, 20 ps, and 81 ps for *n*- (B) and *p*-type (E). Time-dependent kinetics at 478 nm, 494 nm, 514 nm, and 524 nm for *n*-type GaP(100) (C) and at 477 nm, 489 nm, 507 nm, and 521 nm for *p*-type GaP(100)(F).

Fluence-dependent kinetics for *n*- and *p*-type GaP(100). To further elucidate the dynamic nature of surface behaviors, we measured fluence-dependent TR-ESFG kinetics. Figure 3 shows fluence-dependent kinetic traces at 514 nm with PSS polarization for *n*-type (A) and *p*-type (D) GaP(100) under 400 nm photoexcitation from 2.5 to 100 μJ/ cm^2, over 80 ps. The right sides are at a short timescale of 10 ps for clarity. Those for the other three peaks are found in Figure S5. These results show that the transient ESFG signals increase with increasing fluence. The fast process appears to remain unchanged with fluence, while the slow process for both *n*- and *p*-type GaP gets faster with increasing fluence.

To quantitatively understand surface kinetics, the time traces in Figures 3 (A) and (D) were fitted to a doubly exponential function. Figures 3 (C) and (F) show the time constants of both fast component and slow component for *n*-type and *p*-type GaP(100). Maximum transient ESFG change ratios were plotted against fluence at a time delay of 50 ps for *n*- and *p*-type GaP(100), separately, in Figures 3 (B) and (E). The maximum transient signals tend to saturate when the fluence is higher than 20 μJ/cm^2 for both *n*-type and *p*-type GaP(100). The fast process is independent of applied fluence in both cases, suggesting that it is of first-order. This first-order process was attributed to the buildup process of the surface electric fields due to photoinduced charges moving toward the surface. On the other hand, the slow component was attributed to the population of surface carriers in surface states of GaP.

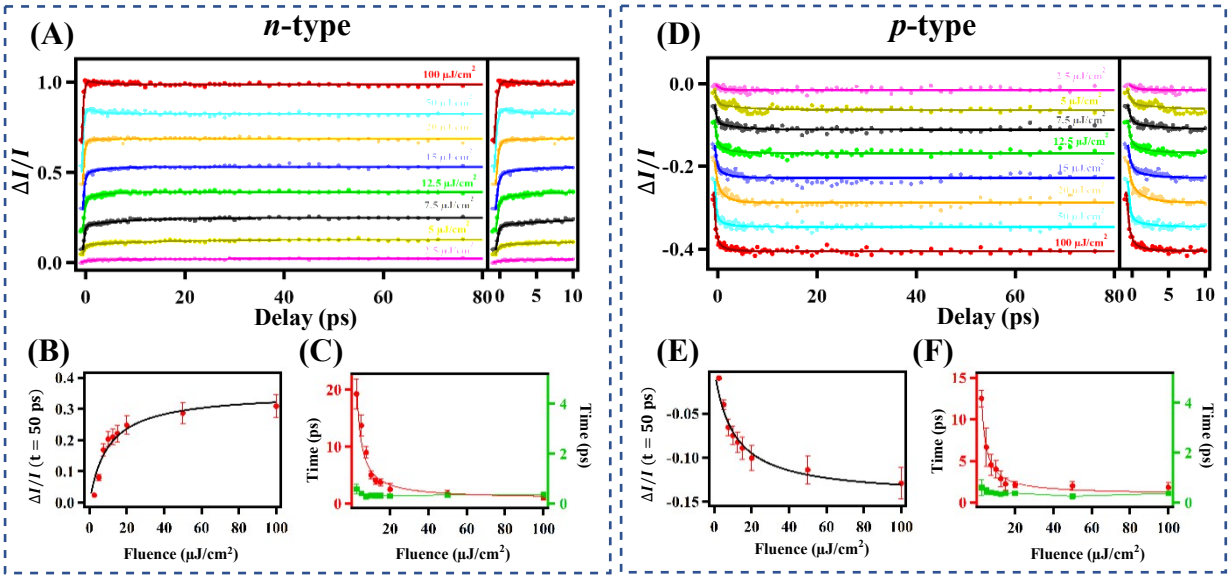

Figure 3. Transient ESFG change, $\frac{\Delta I}{I}$, under 400 nm with PSS polarization as a function of time delay at a probe wavelength of 514 nm for *n*-type (A) and 507 nm for *p*-type (D). The right sides of (A) and (D) are zoomed in at a short time scale. $\frac{\Delta I}{I}$ (t = 50 ps) as a function of the applied fluence for *n*-type (B) and for *p*-type (E). Time constants obtained by fitting of a double exponential function as a function of the applied fluences, for *n*-type (C) and for *p*-type (F).

Our findings reveal different photoinduced buildup of surface electric fields (or surface potentials) and population of the occupancy of surface states in GaP(100) for *n*- and *p*-type GaP. Four surface states were identified at 478 nm, 494 nm, 514 nm, and 524 nm, from shallow to deep with respect to the CB for *n*-type GaP(100). Four surface states at 477 nm, 489 nm, 507 nm, and 521 nm, from shallow to deep with respect to the VB, were also identified for *p*-type GaP(100). According to the electro-neutrality principle., negative-charged surface states for n-type are distributed from just below the conduction band (2.4-2.5 eV above the valence bandedge), while positive-charged surface states for p-type are distributed from just above the valence band (2.4-2.5 eV below the conduction bandedge). These assignements are consistent with those reported in the literature.[98] A sign reversal in transient surface spectra occurs from *n*-type to *p*-type since the surface electric fields result from photogenerated holes or electrons moving towards surface regions for the two dopings. The buildups of surface electric fields are first-order in nature, being similar for *n*- and *p*-type GaP. Conversely, surface population rates, of bimolecular origin, are different for *n*- and *p*-type. The population times of surface states are much slower than those of surface electric field buildup and change with applied fluence. These surface carriers eventually relax via surface recombination with traps or transport into the crystal's bulk.

The band-bending is upward and downward in the depleted surface region for *n*-type and *p*-type GaP, respectively, as schematically shown in Figure 4. Upon photo-illumination, several processes occur at GaP(100) surfaces. Surface electric fields (or surface voltages) are established when free carriers are generated and separated in the space charge region by the incident illumination. The existing surface electric fields, negative for *n*-type and positive for *p*-type, dictate moving directions for photoinduced electrons and holes, leading to the separation of the photoinduced electron−hole pairs. Photoexcited electrons are driven to the bulk region, while photogenerated holes move towards the surface for *n*-type GaP in Figure 4 (A).

The opposite occurs for *p*-type GaP in Figure 4 (B). Surface electric fields are non-specific to all four surface states, shallow or deep, and enhance all transitions of surface states in GaP crystals.

Surface potentials increase with increasing holes at *n*-type GaP surfaces and decrease with increasing electrons at *p*-type GaP surfaces. Such photoinduced surface charging results in the band flattening. Surface voltage follows the relation with carrier density: $V=V_s/(1+ n_s/n)$, where V_s is the band-bending potential, and n_s is the accessible surface carrier density. Considering a penetration depth of 115.9 nm for GaP at 400nm, photogenerated carriers under 10 μJ/cm^2 are on the order of 1.43×10^{13} cm^{-2}. The values of *Vs* were estimated to be 1.05 V and 1.03 V for *n*- and *p*-type GaP, respectively, as found in Supporting Information. Surface band flattening occurs as photoinduced carriers increase. We were then able to obtain the accessible surface carrier densities of $1.41 \pm 0.02\times10^{13}$ and $1.49 \pm 0.02 \times10^{13}$ cm^{-2} for *n*- and *p*-type GaP(100) from the fittings of the relationship between surface voltage and carrier density, as shown in Figures 4 (C) and (D). The obtained surface sites were found to be comparable for *n*- and *p*-type GaP(100), and are consistent with those for the proxy of GaAs.[99]

Surface electric fields (or surface voltages) build up with a rate, $k_{,.,}$ in the space charge region. Photogenerated holes move towards the surface region, resulting in an increase in surface electric fields in the case of *n*-type GaP. On the other hand, photoexcited electrons approach towards the surface region, resulting in a decrease in surface electric fields in the case of *p*-type GaP. Subsequently, surface states are preoccupied with carriers, negative for *n*-type and positive for *p*-type, as presented in Figure 4.[4-5] The surface states with existing charges at equilibrium are populated by photoexcited oppositely-charged carriers with a rate of surface population, $k_{,,'}$ (*i* = *e* or *h*). In other words, the newly generated holes collide with existing electrons in the surface states for *n*-type GaP. Conversely, for *p*-type GaP, the newly generated electrons react with the existing holes in the surface states. It is important to point out that the surface fields are not affected by trapped carriers in surface states in our case since the density of preoccupied oppsite carriers is low from our fitted amplitudes of the kinetics. However, in the case of a high density of preoccupied oppsite carriers, the surface fields might be affect by trapped carriers.

Thus, the dynamical processes of time-dependent surface holes, $n_{,\mathrm{D}}(t)$, and surface electrons, $n_{,\mathrm{E}}(t)$, are described by the following separate differential equations:

$$\frac{4\&_{\mathrm{F_D}}(5)}{45} = k_{,,6}n_{,\mathrm{D}}(t) + k_{7,6}n^{*}_{,\mathrm{D}}(t) - k_{86}n_{,\mathrm{D}}(t) \qquad (5)$$

$$\frac{4\&_{\mathrm{F_E}}(5)}{45} = k_{,,9}n_{,\mathrm{E}}(t) + k_{7,9}n^{*}_{,\mathrm{E}}(t) - k_{89}n_{,\mathrm{E}}(t) \qquad (6)$$

where $k_{,.,'}$ (*i*= *h* or *e*) represents buildup rate of surface electric fields, $k_{7,'}$ (*i*= *h* or *e*) gives the population rates of surface states for holes or electrons, and $k_{8'}$ (*i*= *h* or *e*) is the recombination rate of the electrons or holes trapped on surfaces (beyond our scope since the recombination time is very slow). At a fluence exceeding the saturation value, surface carrier-carrier annihilation can take place, which is not considered here. The surface voltage buildup process has a rate of 2.86 ± 0.30 ps^{-1} for *n*-type and 2.50 ± 0.25 ps^{-1} for *p*-type GaP(100), and is independent of surface states, shallow or deep. The bimolecular process can be considered as a second-order reaction,[92, 100] by following $t_s = t_0 + 1/(k_{p,i}n_0)$, where n_0 is the number density of photoexcited carriers transported to the occupancy of surface states. Therefore, the population rate constants were estimated to be 0.020 ± 0.002 cm^{2}s^{-1} for *n*-type, and 0.035 ± 0.002 cm^{2}s^{-1} for *p*-type, as shown in Figures 4 (C) and (D). These results reveal that the drift velocity of surface electrons is faster than that of surface holes. These differences for GaP are again comparable to those for GaAs.[101]

Previous studies showed that buildups of surface voltages were measured by time-resolved reflectivity experiments with a similar value for *n*- and *p*-type GaAs.[101] The reflectivity for *n*- and *p*-type GaAs exhibited opposite signs for the two different dopings but no spectral information could be obtained. Time-resolved surface-photovoltage spectroscopy (SPV) provided significantly different time constants for *n*- and *p*-type GaAs.[102] Neither time-resolved reflectivity nor time-resolved SPV methods are surface-selective methods. Our surface-specific time-resolved ESFG showed distinct spectral signatures of buildups of surface electric fields for *n*- and *p*- type GaP(100). Furthermore, our TR-ESFG experiments offer unique information of surface carrier population of surface states. Such a process is different from surface recombination, which is on the order of ns-μs for GaP crystals. Surface recombination is concerned about surface carriers interacting with local and deep traps at surfaces, while surface carrier population deals with the interaction of photogenerated surface carriers with preoccupied surface states containing surface charges of an opposite sign. As described above, the classical interpretation says that the shallow surface states can provide free carriers, while the deep surface states are generally localized and act as traps to facilitate the separation of electron-hole pairs. Our results showed that both the delocalized and shallow surface states are involved in the buildup of surface electric fields and surface carrier population.

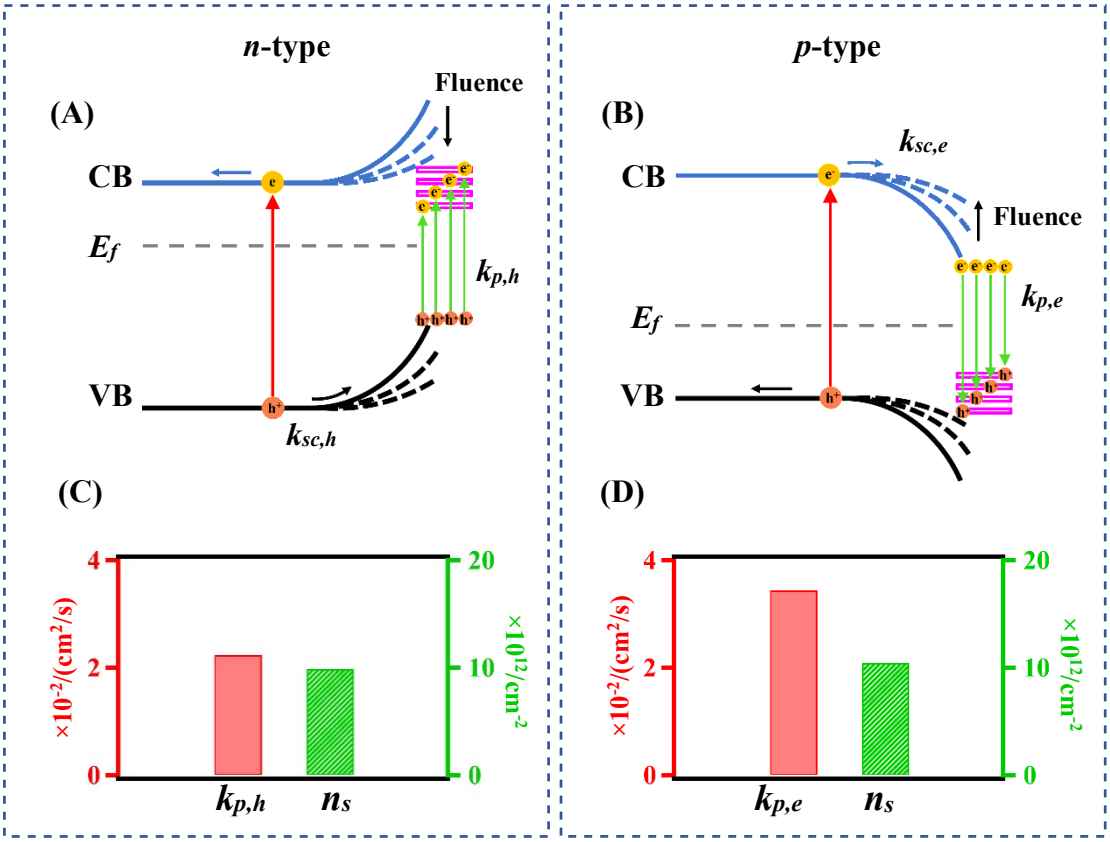

Figure 4. Schematic of photoinduced carriers moving towards surface regions and populating surface states of *n*-type (A) and *p*-type (B) GaP(100) crystals. The arrows represent increasing fluences. The surface population rates and surface densities obtained for *n*- (C) and *p*-type (D) GaP(100).

Conclusions

We have investigated surface electric fields and surface carrier population kinetics for *n*- and *p*-type GaP(100) crystals by deploying time-resolved ESFG spectroscopy. Our azimuth dependent transient ESFG spectra have demonstrated that surface responses, instead of bulk, dominate photoinduced responses. Four surface states were identified at 478 nm, 494 nm, 514 nm, and 524 nm, from shallow to deep with respect to the CB, for *n*-type, and four surface states at 477 nm, 489 nm, 507 nm, and 521 nm, from shallow to deep with respect to the VB, for *p*-type. All of these surface states were found to be involved in both surface electric fields and surface carrier population. Transient spectral signatures of the surface states showed that photoexcited electrons move towards the surface regions for *p*-type GaP, while photoexcited holes migrate to the surface regions for *n*-type GaP. The buildup of the surface electric fields is independent of applied pump fluences with a rate of 2.86 ± 0.30 ps^{-1} for *n*-type and 2.50 ± 0.25 ps^{-1} for *p*-type GaP. Subsequently, the surface carriers populate existing opposite charges in surface states. Such a surface population process is strongly dependent upon applied fluences. The behavior of the surface population process is bimolecular with a rate of 0.020 ± 0.002 cm^{2}s^{-1} for *n*-type, and 0.035 ± 0.002 cm^{2}s^{-1} for *p*-type crystals. These findings

provide new insight into structural dynamics of semiconductor photoelectrode surfaces under ambient conditions.

Supporting Information

The supporting information includes as follows: Steady-state ESFG; Calculations of Fermi levels for *n*- and *p*-type GaP(100); Estimation of Band Bending for *n*- and *p*-type GaP(100); Calculations of Carrier Densities by 400 nm Pump; Nonlinear region caused by large transient changes of time-resolved ESFG; Detection Sensitivity of Time-Resolved ESFG; Azimuth-Dependent Transient ESFG signals under Different Polarizations; Simulated Azimuth-Dependent Pre-factor; Experimental Results of Azimuth-Dependent Transient ESFG signals at t = 90 ps under PSS and SPS Polarization Combinations; Fluence-Dependent Dynamics for the three Peaks under PSS Polarization.

Acknowledgments

This material is based upon work supported by the National Science Foundation under Grant No. [2045084].

Author Contributions

# T.Z. and Z.C.H.F. contributed equally to this work.

References

(1) White, J. L.; Baruch, M. F.; Pander, J. E.; Hu, Y.; Fortmeyer, I. C.; Park, J. E.; Zhang, T.; Liao, K.; Gu, J.; Yan, Y.; et al. Light-Driven Heterogeneous Reduction of Carbon Dioxide: Photocatalysts and Photoelectrodes. *Chem. Rev.* **2015**, *115*, 12888-12935.
(2) Kumar, B.; Llorente, M.; Froehlich, J.; Dang, T.; Sathrum, A.; Kubiak, C. P. Photochemical and Photoelectrochemical Reduction of CO_2. *Annu. Rev. Phys. Chem.* **2012**, *63*, 541-569.
(3) Zhang, N.; Long, R.; Gao, C.; Xiong, Y. Recent Progress on Advanced Design for Photoelectrochemical Reduction of CO_2 to Fuels. *Sci. China. Mater.* **2018**, *61*, 771-805.
(4) Zhang, Z.; Yates Jr, J. T. Band Bending in Semiconductors: Chemical and Physical Consequences at Surfaces and Interfaces. *Chem. Rev.* **2012**, *112*, 5520-5551.
(5) Asubar, J. T.; Yatabe, Z.; Gregusova, D.; Hashizume, T. Controlling Surface/Interface States in Gan-Based Transistors: Surface Model, Insulated Gate, and Surface Passivation. *J. Appl. Phys.* **2021**, *129*, 121102.
(6) Walter, M. G.; Warren, E. L.; McKone, J. R.; Boettcher, S. W.; Mi, Q.; Santori, E. A.; Lewis, N. S. Solar Water Splitting Cells. *Chem. Rev.* **2010**, *110*, 6446-6473.
(7) Guo, L.-J.; Luo, J.-W.; He, T.; Wei, S.-H.; Li, S.-S. Photocorrosion-Limited Maximum Efficiency of Solar Photoelectrochemical Water Splitting. *Phys. Rev. Appl.* **2018**, *10*, 064059.
(8) Habisreutinger, S. N.; Schmidt-Mende, L.; Stolarczyk, J. K. Photocatalytic Reduction of CO_2 on TiO_2 and Other Semiconductors. *Angew. Chem. Int. Ed.* **2013**, *52*, 7372-7408.
(9) Schneider, J.; Matsuoka, M.; Takeuchi, M.; Zhang, J.; Horiuchi, Y.; Anpo, M.; Bahnemann, D. W. Understanding TiO_2 Photocatalysis: Mechanisms and Materials. *Chem. Rev.* **2014**, *114*, 9919-9986.
(10) Pham, T. A.; Ping, Y.; Galli, G. Modelling Heterogeneous Interfaces for Solar Water Splitting. *Nat. Mater.* **2017**, *16*, 401-408.

(11) Upadhyay, R.; Tripathi, M.; Pandey, A. Surface Modification of Semiconductor Photoelectrodes for Better Photoelectrochemical Performance. *High Energy Chem.* **2013**, *47*, 308-314.
(12) Corby, S.; Pastor, E.; Dong, Y.; Zheng, X.; Francàs, L.; Sachs, M.; Selim, S.; Kafizas, A.; Bakulin, A. A.; Durrant, J. R. Charge Separation, Band-Bending, and Recombination in WO_3 Photoanodes. *J. Phys. Chem. Lett.* **2019**, *10*, 5395-5401.
(13) Yang, H. A Short Review on Heterojunction Photocatalysts: Carrier Transfer Behavior and Photocatalytic Mechanisms. *Mater. Res. Bull.* **2021**, *142*, 111406.
(14) Young, K. M. H.; Klahr, B. M.; Zandi, O.; Hamann, T. W. Photocatalytic Water Oxidation with Hematite Electrodes. *Catal. Sci. Technol.* **2013**, *3*, 1660-1671.
(15) Kovačič, Ž.; Likozar, B.; Huš, M. Photocatalytic CO_2 Reduction: A Review of Ab Initio Mechanism, Kinetics, and Multiscale Modeling Simulations. *ACS Catal.* **2020**, *10*, 14984-15007.
(16) Liu, L.; Li, Y. Understanding the Reaction Mechanism of Photocatalytic Reduction of CO_2 with H_2O on TiO_2-Based Photocatalysts: A Review. *Aerosol and Air Qual. Res.* **2014**, *14*, 453-469.
(17) Miller, G. L.; Lang, D. V.; Kimerling, L. C. Capacitance Transient Spectroscopy. *Annu. Rev. Mater. Sci.* **1977**, *7*, 377-448.
(18) Langer, J. M.; Heinrich, H. Deep-Level Impurities: A Possible Guide to Prediction of Band-Edge Discontinuities in Semiconductor Heterojunctions. *Phys. Rev. Lett.* **1985**, *55*, 1414-1417.
(19) Stiévenard, D.; Feng, S. L. Defects in Heterostructures and Superlattices. *Mater. Sci. Forum* **1989**, *38-41*, 679-688.
(20) Lou, Z.; Wang, P.; Huang, B.; Dai, Y.; Qin, X.; Zhang, X.; Wang, Z.; Liu, Y. Enhancing Charge Separation in Photocatalysts with Internal Polar Electric Fields. *ChemPhotoChem* **2017**, *1*, 136-147.
(21) Kamat, P. V. Manipulation of Charge Transfer across Semiconductor Interface. A Criterion That Cannot Be Ignored in Photocatalyst Design. *J. Phys. Chem. Lett.* **2012**, *3*, 663-672.
(22) Yang, J.; Wang, D.; Han, H.; Li, C. Roles of Cocatalysts in Photocatalysis and Photoelectrocatalysis. *Acc. Chem. Res.* **2013**, *46*, 1900-1909.
(23) Linsebigler, A. L.; Lu, G.; Yates, J. T. Photocatalysis on TiO_2 Surfaces: Principles, Mechanisms, and Selected Results. *Chem. Rev.* **1995**, *95*, 735-758.
(24) Halmann, M. Photoelectrochemical Reduction of Aqueous Carbon Dioxide on p-Type Gallium Phosphide in Liquid Junction Solar Cells. *Nature* **1978**, *275*, 115-116.
(25) Zeng, G.; Qiu, J.; Li, Z.; Pavaskar, P.; Cronin, S. B. CO_2 Reduction to Methanol on TiO_2-Passivated GaP Photocatalysts. *ACS Catal.* **2014**, *4*, 3512-3516.
(26) Inoue, T.; Fujishima, A.; Konishi, S.; Honda, K. Photoelectrocatalytic Reduction of Carbon Dioxide in Aqueous Suspensions of Semiconductor Powders. *Nature* **1979**, *277*, 637-638.
(27) Barton, E. E.; Rampulla, D. M.; Bocarsly, A. B. Selective Solar-Driven Reduction of CO_2 to Methanol Using a Catalyzed p-GaP Based Photoelectrochemical Cell. *J. Am. Chem. Soc.* **2008**, *130*, 6342-6344.
(28) Taniguchi, Y.; Yoneyama, H.; Tamura, H. Photoelectrochemical Reduction of Carbon Dioxide at p-Type Gallium Phosphide Electrodes in the Presence of Crown Ether. *Bull. Chem. Soc. Jpn.* **1982**, *55*, 2034-2039.
(29) Hamilton, B.; Peaker, A. R.; Wight, D. R. Deep-State-Controlled Minority-Carrier Lifetime in n-Type Gallium Phosphide. *J. Appl. Phys.* **1979**, *50*, 6373-6385.

(30) Lubberhuizen, W. H.; Vanmaekelbergh, D.; Van Faassen, E. Recombination of Photogenerated Charge Carriers in Nanoporous Gallium Phosphide. *J. Porous Mater.* **2000**, *7*, 147-152.
(31) Ichihashi, F.; Kawaguchi, T.; Dong, X.; Kuwahara, M.; Ito, T.; Harada, S.; Tagawa, M.; Ujihara, T. Temperature Dependence of Carrier Relaxation Time in Gallium Phosphide Evaluated by Photoemission Measurements. *AIP Adv.* **2017**, *7*, 115314.
(32) Grinblat, G.; Zhang, H.; Nielsen Michael, P.; Krivitsky, L.; Berté, R.; Li, Y.; Tilmann, B.; Cortés, E.; Oulton Rupert, F.; Kuznetsov Arseniy, I.; et al. Efficient Ultrafast All-Optical Modulation in a Nonlinear Crystalline Gallium Phosphide Nanodisk at the Anapole Excitation. *Sci. Adv.* **2020**, *6*, eabb3123.
(33) Shen, Y. R. Surface Properties Probed by Second-Harmonic and Sum-Frequency Generation. *Nature* **1989**, *337*, 519-525.
(34) Eisenthal, K. B. Photochemistry and Photophysics of Liquid Interfaces by Second Harmonic Spectroscopy. *J. Phys. Chem.* **1996**, *100*, 12997-13006.
(35) Eisenthal, K. B. Liquid Interfaces Probed by Second-Harmonic and Sum-Frequency Spectroscopy. *Chem. Rev.* **1996**, *96*, 1343-1360.
(36) Miranda, P. B.; Shen, Y. R. Liquid Interfaces: A Study by Sum-Frequency Vibrational Spectroscopy. *J. Phys. Chem. B* **1999**, *103*, 3292-3307.
(37) Chen, Z.; Shen, Y.; Somorjai, G. A. Studies of Polymer Surfaces by Sum Frequency Generation Vibrational Spectroscopy. *Annu. Rev. Phys. Chem.* **2002**, *53*, 437-465.
(38) Richmond, G. L. Molecular Bonding and Interactions at Aqueous Surfaces as Probed by Vibrational Sum Frequency Spectroscopy. *Chem. Rev.* **2002**, *102*, 2693-2724.
(39) Wang, H. F.; Gan, W.; Lu, R.; Rao, Y.; Wu, B. H. Quantitative Spectral and Orientational Analysis in Surface Sum Frequency Generation Vibrational Spectroscopy (SFG-VS). *Int. Rev. Phys. Chem.* **2005**, *24*, 191-256.
(40) Geiger, F. M. Second Harmonic Generation, Sum Frequency Generation, and $\chi^{(3)}$: Dissecting Environmental Interfaces with a Nonlinear Optical Swiss Army Knife. *Annu. Rev. Phys. Chem.* **2009**, *60*, 61-83.
(41) Arnolds, H.; Bonn, M. Ultrafast Surface Vibrational Dynamics. *Surf. Sci. Rep.* **2010**, *65*, 45-66.
(42) Jubb, A. M.; Hua, W.; Allen, H. C. Environmental Chemistry at Vapor/Water Interfaces: Insights from Vibrational Sum Frequency Generation Spectroscopy. *Annu. Rev. Phys. Chem.* **2012**, *63*, 107-130.
(43) Johnson, C. M.; Baldelli, S. Vibrational Sum Frequency Spectroscopy Studies of the Influence of Solutes and Phospholipids at Vapor/Water Interfaces Relevant to Biological and Environmental Systems. *Chem. Rev.* **2014**, *114*, 8416-8446.
(44) Yan, E. C. Y.; Fu, L.; Wang, Z. G.; Liu, W. Biological Macromolecules at Interfaces Probed by Chiral Vibrational Sum Frequency Generation Spectroscopy. *Chem. Rev.* **2014**, *114*, 8471-8498.
(45) Berne, B. J.; Fourkas, J. T.; Walker, R. A.; Weeks, J. D. Nitriles at Silica Interfaces Resemble Supported Lipid Bilayers. *Acc. Chem. Res.* **2016**, *49*, 1605-1613.
(46) Elsenbeck, D.; Das, S. K.; Velarde, L. Substrate Influence on the Interlayer Electron–Phonon Couplings in Fullerene Films Probed with Doubly-Resonant SFG Spectroscopy. *Phys. Chem. Chem. Phys.* **2017**, *19*, 18519-18528.

(47) Stiopkin, I. V.; Weeraman, C.; Pieniazek, P. A.; Shalhout, F. Y.; Skinner, J. L.; Benderskii, A. V. Hydrogen Bonding at the Water Surface Revealed by Isotopic Dilution Spectroscopy. *Nature* **2011**, *474*, 192-195.
(48) Mizuno, H.; Rizzuto, A. M.; Saykally, R. J. Charge-Transfer-to-Solvent Spectrum of Thiocyanate at the Air/Water Interface Measured by Broadband Deep Ultraviolet Electronic Sum Frequency Generation Spectroscopy. *J. Phys. Chem. Lett.* **2018**, *9*, 4753-4757.
(49) Moon, A. P.; Pandey, R.; Bender, J. A.; Cotton, D. E.; Renard, B. A.; Roberts, S. T. Using Heterodyne-Detected Electronic Sum Frequency Generation to Probe the Electronic Structure of Buried Interfaces. *J. Phys. Chem. C* **2017**, *121*, 18653-18664.
(50) Li, Y. M.; Wang, J. M.; Xiong, W. Probing Electronic Structures of Organic Semiconductors at Buried Interfaces by Electronic Sum Frequency Generation Spectroscopy. *J. Phys. Chem. C* **2015**, *119*, 28083-28089.
(51) Watson, B. R.; Doughty, B.; Calhoun, T. R. Energetics at the Surface: Direct Optical Mapping of Core and Surface Electronic Structure in Cdse Quantum Dots Using Broadband Electronic Sum Frequency Generation Microspectroscopy. *Nano Lett.* **2019**, *19*, 6157-6165.
(52) Roke, S.; Roeterdink, W. G.; Wijnhoven, J. E.; Petukhov, A. V.; Kleyn, A. W.; Bonn, M. Vibrational Sum Frequency Scattering from a Submicron Suspension. *Phys. Rev. Lett.* **2003**, *91*, 258302.
(53) Wang, C. Y.; Groenzin, H.; Shultz, M. J. Surface Characterization of Nanoscale TiO_2 Film by Sum Frequency Generation Using Methanol as a Molecular Probe. *J. Phys. Chem. B* **2004**, *108*, 265-272.
(54) Kung, K. Y.; Chen, P.; Wei, F.; Shen, Y. R.; Somorjai, G. A. Sum-Frequency Generation Spectroscopic Study of CO Adsorption and Dissociation on Pt(111) at High Pressure and Temperature. *Surf. Sci.* **2000**, *463*, L627-L633.
(55) Makarem, M.; Lee, C. M.; Sawada, D.; O'Neill, H. M.; Kim, S. H. Distinguishing Surface Versus Bulk Hydroxyl Groups of Cellulose Nanocrystals Using Vibrational Sum Frequency Generation Spectroscopy. *J. Phys. Chem. Lett.* **2017**, *9*, 70-75.
(56) Vanselous, H.; Stingel, A. M.; Petersen, P. B. Interferometric 2D Sum Frequency Generation Spectroscopy Reveals Structural Heterogeneity of Catalytic Monolayers on Transparent Materials. *J. Phys. Chem. Lett.* **2017**, *8*, 825-830.
(57) Wang, H. Y.; Gao, T.; Xiong, W. Self-Phase-Stabilized Heterodyne Vibrational Sum Frequency Generation Microscopy. *ACS Photonics* **2017**, *4*, 1839-1845.
(58) Laaser, J. E.; Zanni, M. T. Extracting Structural Information from the Polarization Dependence of One- and Two-Dimensional Sum Frequency Generation Spectra. *J. Phys. Chem. A* **2013**, *117*, 5875-5890.
(59) Liljeblad, J. F.; Tyrode, E. Vibrational Sum Frequency Spectroscopy Studies at Solid/Liquid Interfaces: Influence of the Experimental Geometry in the Spectral Shape and Enhancement. *J. Phys. Chem. C* **2012**, *116*, 22893-22903.
(60) Chowdhury, A. U.; Liu, F.; Watson, B. R.; Ashkar, R.; Katsaras, J.; Patrick Collier, C.; Lutterman, D. A.; Ma, Y.-Z.; Calhoun, T. R.; Doughty, B. Flexible Approach to Vibrational Sum-Frequency Generation Using Shaped Near-Infrared Light. *Opt. Lett.* **2018**, *43*, 2038-2041.
(61) Rey, N. G.; Dlott, D. D. Studies of Electrochemical Interfaces by Broadband Sum Frequency Generation. *J. Electroanal. Chem.* **2017**, *800*, 114-125.
(62) Anglin, T. C.; Conboy, J. C. Kinetics and Thermodynamics of Flip-Flop in Binary Phospholipid Membranes Measured by Sum-Frequency Vibrational Spectroscopy. *Biochemistry* **2009**, *48*, 10220-10234.

(63) Wen, Y.-C.; Zha, S.; Liu, X.; Yang, S.; Guo, P.; Shi, G.; Fang, H.; Shen, Y. R.; Tian, C. Unveiling Microscopic Structures of Charged Water Interfaces by Surface-Specific Vibrational Spectroscopy. *Phys. Rev. Lett.* **2016**, *116*, 016101.
(64) Feng, R.-J.; Lin, L.; Li, Y.-Y.; Liu, M.-H.; Guo, Y.; Zhang, Z. Effect of Ca^{2+} to Sphingomyelin Investigated by Sum Frequency Generation Vibrational Spectroscopy. *Biophys. J* . **2017**, *112*, 2173-2183.
(65) Liu, S.; Liu, A.-a.; Wen, B.; Zhang, R.; Zhou, C.; Liu, L.-M.; Ren, Z. Coverage Dependence of Methanol Dissociation on TiO_2 (110). *J. Phys. Chem. Lett.* **2015**, *6*, 3327-3334.
(66) Zhang, Z.; Kim, J.; Khoury, R.; Saghayezhian, M.; Haber, L. H.; Plummer, E. Surface Sum Frequency Generation Spectroscopy on Non-Centrosymmetric Crystal GaAs (001). *Surf. Sci.* **2017**, *664*, 21-28.
(67) Xu, B.; Wu, Y.; Sun, D.; Dai, H.-L.; Rao, Y. Stabilized Phase Detection of Heterodyne Sum Frequency Generation for Interfacial Studies. *Opt. Lett.* **2015**, *40*, 4472-4475.
(68) Rao, Y.; Hong, S.-Y.; Turro, N. J.; Eisenthal, K. B. Molecular Orientational Distribution at Interfaces Using Second Harmonic Generation. *J. Phys. Chem. C* **2011**, *115*, 11678-11683.
(69) Rao, Y.; Comstock, M.; Eisenthal, K. B. Absolute Orientation of Molecules at Interfaces. *J. Phys. Chem. B* **2006**, *110*, 1727-1732.
(70) Park, H.; Gutierrez, M.; Wu, X.; Kim, W.; Zhu, X.-Y. Optical Probe of Charge Separation at Organic/Inorganic Semiconductor Interfaces. *J. Phys. Chem. C* **2013**, *117*, 10974-10979.
(71) Nelson, C.; Luo, J.; Jen, A.-Y.; Laghumavarapu, R.; Huffaker, D.; Zhu, X.-Y. Time-, Energy-, and Phase-Resolved Second-Harmonic Generation at Semiconductor Interfaces. *J. Phys. Chem. C* **2014**, *118*, 27981-27988.
(72) Goodman, A. J.; Dahod, N. S.; Tisdale, W. A. Ultrafast Charge Transfer at a Quantum Dot/2D Materials Interface Probed by Second Harmonic Generation. *J. Phys. Chem. Lett.* **2018**, *9*, 4227-4232.
(73) Tisdale, W. A.; Williams, K. J.; Timp, B. A.; Norris, D. J.; Aydil, E. S.; Zhu, X.-Y. Hot-Electron Transfer from Semiconductor Nanocrystals. *Science* **2010**, *328*, 1543-1547.
(74) Sitzmann, E. V.; Eisenthal, K. B. Dynamics of Intermolecular Electronic Energy Transfer at an Air/Liquid Interface. *J. Chem. Phys.* **1989**, *90*, 2831-2832.
(75) Castro, A.; Sitzmann, E. V.; Zhang, D.; Eisenthal, K. B. Rotational Relaxation at the Air/Water Interface by Time-Resolved Second Harmonic Generation. *J. Phys. Chem.* **1991**, *95*, 6752-6753.
(76) Shi, X.; Borguet, E.; Tarnovsky, A. N.; Eisenthal, K. B. Ultrafast Dynamics and Structure at Aqueous Interfaces by Second Harmonic Generation. *Chem. Phys.* **1996**, *205*, 167-178.
(77) Zimdars, D.; Dadap, J. I.; Eisenthal, K. B.; Heinz, T. F. Anisotropic Orientational Motion of Molecular Adsorbates at the Air−Water Interface. *J. Phys. Chem. B* **1999**, *103*, 3425-3433.
(78) Zimdars, D.; Dadap, J. I.; Eisenthal, K. B.; Heinz, T. F. Femtosecond Dynamics of Solvation at the Air/Water Interface. *Chem. Phys. Lett.* **1999**, *301*, 112-120.
(79) Zimdars, D.; Eisenthal, K. B. Effect of Solute Orientation on Solvation Dynamics at the Air/Water Interface. *J. Phys. Chem. A* **1999**, *103*, 10567-10570.
(80) Benderskii, A. V.; Eisenthal, K. B. Effect of Organic Surfactant on Femtosecond Solvation Dynamics at the Air-Water Interface. *J. Phys. Chem. B* **2000**, *104*, 11723-11728.
(81) Benderskii, A. V.; Eisenthal, K. B. Aqueous Solvation Dynamics at the Anionic Surfactant Air/Water Interface. *J. Phys. Chem. B* **2001**, *105*, 6698-6703.

(82) Shang, X.; Benderskii, A. V.; Eisenthal, K. B. Ultrafast Solvation Dynamics at Silica/Liquid Interfaces Probed by Time-Resolved Second Harmonic Generation. *J. Phys. Chem. B* **2001**, *105*, 11578-11585.
(83) Zimdars, D.; Eisenthal, K. B. Static and Dynamic Solvation at the Air/Water Interface. *J. Phys. Chem. B* **2001**, *105*, 3993-4002.
(84) Benderskii, A. V.; Eisenthal, K. B. Dynamical Time Scales of Aqueous Solvation at Negatively Charged Lipid/Water Interfaces. *J. Phys. Chem. A* **2002**, *106*, 7482-7490.
(85) Benderskii, A. V.; Henzie, J.; Basu, S.; Shang, X.; Eisenthal, K. B. Femtosecond Aqueous Solvation at a Positively Charged Surfactant/Water Interface. *J. Phys. Chem. B* **2004**, *108*, 14017-14024.
(86) McArthur, E. A.; Eisenthal, K. B. Ultrafast Excited-State Electron Transfer at an Organic Liquid/Aqueous Interface. *J. Am. Chem. Soc.* **2006**, *128*, 1068-1069.
(87) Nguyen, K. T.; Shang, X.; Eisenthal, K. B. Molecular Rotation at Negatively Charged Surfactant/Aqueous Interfaces. *J. Phys. Chem. B* **2006**, *110*, 19788-19792.
(88) Shang, X.; Nguyen, K.; Rao, Y.; Eisenthal, K. B. In-Plane Molecular Rotational Dynamics at a Negatively Charged Surfactant/Aqueous Interface. *J. Phys. Chem. C* **2008**, *112*, 20375-20381.
(89) Rao, Y.; Song, D.; Turro, N. J.; Eisenthal, K. B. Orientational Motions of Vibrational Chromophores in Molecules at the Air/Water Interface with Time-Resolved Sum Frequency Generation. *J. Phys. Chem. B* **2008**, *112*, 13572-13576.
(90) Rao, Y.; Xu, M.; Jockusch, S.; Turro, N. J.; Eisenthal, K. B. Dynamics of Excited State Electron Transfer at a Liquid Interface Using Time-Resolved Sum Frequency Generation. *Chem. Phys. Lett.* **2012**, *544*, 1-6.
(91) Rao, Y.; Qian, Y.; Deng, G.-H.; Kinross, A.; Turro, N. J.; Eisenthal, K. B. Molecular Rotation in 3 Dimensions at an Air/Water Interface Using Femtosecond Time Resolved Sum Frequency Generation. *J. Chem. Phys.* **2019**, *150*, 094709.
(92) Deng, G.-H.; Qian, Y.; Rao, Y. Development of Ultrafast Broadband Electronic Sum Frequency Generation for Charge Dynamics at Surfaces and Interfaces. *J. Chem. Phys.* **2019**, *150*, 024708.
(93) Nihonyanagi, S.; Yamaguchi, S.; Tahara, T. Ultrafast Dynamics at Water Interfaces Studied by Vibrational Sum Frequency Generation Spectroscopy. *Chem. Rev.* **2017**, *117*, 10665-10693.
(94) Deng, G.-H.; Qian, Y.; Wei, Q.; Zhang, T.; Rao, Y. Interface-Specific Two-Dimensional Electronic Sum Frequency Generation Spectroscopy. *J. Phys. Chem. Lett.* **2020**, *11*, 1738-1745.
(95) Deng, G.-H.; Wei, Q.; Qian, Y.; Zhang, T.; Leng, X.; Rao, Y. Development of Interface-/Surface-Specific Two-Dimensional Electronic Spectroscopy. *Rev. Sci. Instrum.* **2021**, *92*, 023104.
(96) Sekiguchi, K.; Yamaguchi, S.; Tahara, T. Femtosecond Time-Resolved Electronic Sum-Frequency Generation Spectroscopy: A New Method to Investigate Ultrafast Dynamics at Liquid Interfaces. *J. Chem. Phys.* **2008**, *128*, 114715.
(97) Sen, P.; Yamaguchi, S.; Tahara, T. Ultrafast Dynamics of Malachite Green at the Air/Water Interface Studied by Femtosecond Time-Resolved Electronic Sum Frequency Generation (TR-ESFG): An Indicator for Local Viscosity. *Faraday Discuss.* **2010**, *145*, 411-428.
(98) Uchida, H.; Yoneyama, H.; Tamura, H., Surface States Formation Due to Impregnated Hydrogen at P-Type Gallium Phosphide Electrodes with Metal Adatoms. *J. Electrochem. Soc.* **1980**, *127*, 99-104.

(99) Zhou, X.; Hsiang, T. Y.; Miller, R. J. D. Monte Carlo Study of Photogenerated Carrier Transport in Gaas Surface Space-Charge Fields. *J. Appl. Phys.* **1989**, *66*, 3066-3073.
(100) Atkins, P.; Paula, J. d. *Atkins' Physical Chemistry*; Oxford University Press: New York, 2002.
(101) Dekorsy, T.; Pfeifer, T.; Kütt, W.; Kurz, H. Subpicosecond Carrier Transport in GaAs Surface-Space-Charge Fields. *Phys. Rev. B* **1993**, *47*, 3842.
(102) Cavalcoli, D.; Cavallini, A. Surface Photovoltage Spectroscopy-Method and Applications. *Phys. Status Solidi C* **2010**, *7*, 1293-1300.

TOC Graphic